applied optics

Performance of an optical encoder based on a nondiffractive beam implemented with a specific photodetection integrated circuit and a diffractive optical element

Fernando Perez Quintián,[1,2,*] Nicolás Calarco,[1] Ariel Lutenberg,[2,3] and José Lipovetzky[2,4]

[1]Facultad de Ingeniería, Universidad Nacional del Comahue, 1400 Buenos Aires St., Neuquén Q8300IBX, Argentina
[2]Consejo Nacional de Investigaciones Científicas y Técnicas (CONICET), Av. Rivadavia 1917 (C1033AAJ), Ciudad Autónoma de Buenos Aires, Argentina
[3]Facultad de Ingeniería, Universidad de Buenos Aires, 850 Paseo Colón Av., Ciudad de Buenos Aires C1063ACV, Argentina
[4]Gerencia de Física, Centro Atómico Bariloche, Comisión Nacional de Energía Atómica (CNEA), Avda. E. Bustillo 9500, 8400 Bariloche, Argentina
*Corresponding author: fernando.perezq@fain.uncoma.edu.ar

Received 16 June 2015; revised 7 August 2015; accepted 9 August 2015; posted 10 August 2015 (Doc. ID 242895); published 26 August 2015

In this paper, we study the incremental signal produced by an optical encoder based on a nondiffractive beam (NDB). The NDB is generated by means of a diffractive optical element (DOE). The detection system is composed by an application specific integrated circuit (ASIC) sensor. The sensor consists of an array of eight concentric annular photodiodes, each one provided with a programmable gain amplifier. In this way, the system is able to synthesize a nonuniform detectivity. The contrast, amplitude, and harmonic content of the sinusoidal output signal are analyzed. The influence of the cross talk among the annular photodiodes is placed in evidence through the dependence of the signal contrast on the wavelength.

OCIS codes: (120.4570) Optical design of instruments; (120.3930) Metrological instrumentation; (040.5160) Photodetectors; (120.3940) Metrology; (050.1950) Diffraction gratings.

http://dx.doi.org/10.1364/AO.54.007640

1. INTRODUCTION

Optical encoders are rotation or linear displacement sensors that reach submicrometric resolution and are used in a wide variety of equipment such as printers, lathes, radars, robots, satellites, etc. There are several optical encoder designs, but all of them rely on the movement of an optical head with respect to a fixed scale [1–15]. The optical head includes one or more light sources that shed some kind of structured light beam, which is shaped by the scale. The shaped light beam, transmitted or reflected by the scale, is then detected by an array of photodetectors or by a monolithic photodetector with a secondary scale pattern as a mask. Finally, an electronic circuit generates a signal related to the variation of the collected light that encodes the displacement of the optical head relative to the scale. More specifically, incremental encoders typically use four detectors to produce four identical sinusoidal signals, 90° out of phase of each other. This makes it possible to determine the moving direction and reduce the effects of any light intensity change [16,17].

In general, optical encoders are multiple grating systems; the most frequent configurations of grating systems are Moiré [1,2], Lau [3,4], and generalized grating imaging [4,5]. The scale is usually a chrome on glass grating. However, steel tape gratings are used for measuring displacements longer than 3 m. The influence of the steel roughness on the encoder performance for the aforementioned grating configurations has been studied [6]. Besides these common optical encoders, there are others based on interferential diffractive [7–9] and alternative [10–13] designs.

There are continual contributions to the field of optical encoders based on achieving improvements in one of the following key aspects: resolution, stability, size, and cost. For example, in some of the more recent referenced papers, the emphasis is on the size and cost through a design using embedded gratings and a passive alignment system [14] and through clever integration of the structured light source and the four photodetectors with their masks on a monolithic Si substrate [15].

In 2008, we proposed an optical encoder based on a nondiffractive beam (NDB) [13] and presented some experimental results and a theoretical model to understand, analyze, and optimize its performance [18,19]. The main characteristic of this design is its excellent stability, which is due to the propagation invariance of the NDBs, thus allowing higher tolerances under variations in the distance between the scale and the moving

head. The proposed design also allows high resolution thanks to its low harmonic content in the output signal, which allows precise electronic interpolation.

This work is intended to demonstrate that the optical encoder based on NDBs is able to accomplish the two other wishful characteristics of an optical encoder: low cost and small size. For that purpose, we study one of the four necessary incremental signals produced by the proposed encoder head implemented on a 20 μm pitch grating scale. The NDB is generated by an amplitude mask diffractive optical element (DOE), and the detection system is a specially designed programmable CMOS integrated circuit sensor [20].

In the next section, we introduce the basis of the operating principle of the encoder design that generates the incremental signals. Then, we describe the experimental setup and, in particular, the characteristics of the DOE and the programmable CMOS integrated circuit sensor. Section 4 presents the experimental results together with an exhaustive analysis of each. Finally, we summarize the conclusions of this work.

2. OPERATION PRINCIPLE OF THE ENCODER

The scheme of the NDB encoder is shown in Fig. 1. A beam from a laser diode (LD) impinges on the DOE, which is designed to produce a zero-order Bessel beam, that is, the NDB. The NDB is transmitted through the scale, which is a 20 μm pitch Ronchi grating. After this, the diffracted beam impinges on the photodetector (PD). The LD, DOE, and PD constitute the moving head, and the scale is fixed.

To obtain an analytical expression for the output signal, we will describe the electric field at the photodetector in the theoretical framework of the scalar diffraction theory through the propagation of the angular spectrum of plane waves. Polarization effects, therefore, are not included, as is usually done in theoretical treatments of double grating systems, and they are not a main cause of metrological errors in optical encoders [21]. Regarding the polarization in connection to the NDB, according to Bouchal and Olivik [22] the influence of the z polarization of the light in the Bessel beam is negligible for the angles involved here.

The electric field at the photodetector plane is given by [19]

$$E(x, y, z, \Delta x) \propto \mathrm{FT}^{-1}\{\{\mathrm{FT}[t_G(x-\Delta x)] \otimes \mathrm{FT}[J_0(x, y)]\} \cdot \mathrm{H}(f_x, f_y, z)\}. \quad (1)$$

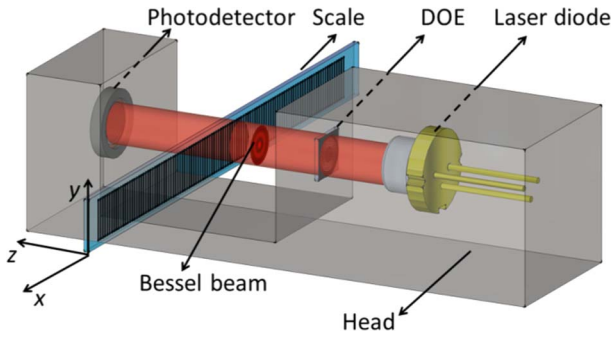

Fig. 1. Scheme of the optical encoder based on a nondiffractive beam.

The equation indicates that the zero-order Bessel beam $J_0(x, y)$ produced by the DOE propagates in the z direction without changing its profile until it reaches the grating whose transmittance is the grating transmittance $t_G(x)$ shifted by an amount Δx, which is the relative movement between the optical head and the grating. The transmitted field in the frequency domain is the convolution of the respective Fourier transforms (FT). Then, the propagation of the transmitted field is modeled in the frequency domain by the linear filter $\mathrm{H}(f_x, f_y, z)$ [23] with a finite bandwidth:

$$\mathrm{H}(f_x, f_y, z) = \exp\left[i2\pi\frac{\lambda}{z}\sqrt{1-(\lambda f_x)^2-(\lambda f_y)^2}\right]. \quad (2)$$

Therefore, the signal obtained at the photodetector output will be proportional to

$$s(z, \Delta x) \propto \iint \|E(x, y, z, \Delta x)\|^2 d(x, y)\mathrm{d}x\mathrm{d}y, \quad (3)$$

where we have integrated the intensity at the detector, assuming it has nonuniform detectivity, $d(x, y)$. This integral can be solved in the frequency domain using the Parseval theorem:

$$s(z, \Delta x) \propto \iint \|\{\{\mathrm{FT}[t_G(x-\Delta x)] \otimes \mathrm{FT}[J_0(x, y)]\}\mathrm{H}(f_x, f_y)\} \otimes \mathrm{FT}[\sqrt{d(x, y)}]\|^2 \mathrm{d}f_x\mathrm{d}f_y. \quad (4)$$

In the discussions held in [20] about the functional forms of the FT involved in Eq. (4), it was clear that the best functional form of $d(x, y)$ would be one that the FT of its square root had circular symmetry and no tails, which is, clearly, a *circ* function in the frequency domain, which is a *besinc* function in the spatial domain [23]. Therefore, the signal will be improved if we use a detector with a besinc^2 detectivity:

$$d(x, y) = \left[2\frac{J_1(\pi\sqrt{x^2+y^2}/a)}{\pi\sqrt{x^2+y^2}/a}\right]^2, \quad (5)$$

where a is a parameter that determines the detector size.

Under these ideal conditions, a sinusoidal electronic signal $s(\Delta x)$ with the same period as the grating is obtained. Thus, a relative head displacement of one grating period generates one period of the signal. In this way, the intrinsic resolution of the system is the grating pitch. However, this resolution could be electronically improved if a set of four 90° phase-shifted sinusoidal signals with low harmonic distortion are generated, say, s_1, s_2, s_3, and s_4. As is usual in optical encoders, two zero mean quadrature signals are obtained from them, $s_A = s_1 - s_3 = A\sin(2\pi\frac{\Delta x}{p})$ and $s_B = s_2 - s_4 = A\cos(2\pi\frac{\Delta x}{p})$, where p is the grating period. With these two signals, the relative displacement is determined:

$$\Delta x = \frac{p}{2\pi}\tan^{-1}\left(\frac{s_A}{s_B}\right). \quad (6)$$

Therefore, an electronic unit can be used to accurately measure relative displacements as small as a hundredth of the grating pitch, depending on the quality of the signals s_A and s_B. The relative phase-shifts, amplitudes, offsets, and harmonic distortions of the signals s_1, s_2, s_3, and s_4 play a relevant role in the accuracy of the electronic interpolation of the displacements [21].

The aim of the rest of this work is to exhaustively analyze the signal $s(\Delta x)$ obtained with the experimental configuration of Fig. 1.

3. EXPERIMENTAL SETUP

The scheme of the experimental setup mounted in the laboratory is shown in Fig. 1. The laser diode, the DOE, and the photodetection integrated circuit constitutes the encoder head and were fixed in the experiment. The relative displacement Δx between the scale and the head was controlled by a linear motorized stage with 0.2 μm resolution where the scale was attached. The distance z between the scale and the photodetector could be varied, and two different laser diodes with wavelengths of 635 and 405 nm were used.

The two key elements in the configuration are the DOE and the photodetector. Hence, they are described with more detail in the two following subsections.

A. Diffractive Optical Element

There are several types of NDB [24], but, in a previous work [19], we showed that the best performance of the encoder is achieved with a zero-order Bessel beam. This NDB can be produced with an axicon and a slit-lens system, for example [25–27]. For reasons of cost and size of the component, we decided to use a DOE consisting of an amplitude binary mask of concentric rings, as shown in Fig. 2.

The pitch of this radial grating is 40 μm and has only five rings, being the diameter of the more external ring 0.8 mm. The center is black to avoid the interference between zero- and first-order diffracted fields at the propagation axis. The interference of the first-order diffracted rays produces the zero-order Bessel beam at the propagation axis, and its intensity pattern is independent of the wavelength of the incident light.

The fields produced by illuminating this DOE with a plane wave at different distances were calculated using the propagation of the angular spectrum and compared with the exact zero-order Bessel beam. The results are shown in Fig. 3 for $\lambda = 635$ nm. The simulated NDB has a correlation coefficient of 0.9 (after 18 mm of propagation distance) with the theoretical NDB function,

$$\left[J_0\left(2.405\sqrt{x^2+y^2}/r_0\right)\right]^2, \tag{7}$$

for $r_0 = 15.5$ μm, where r_0 is the first zero of Eq. (7). The value of r_0 is chosen depending on the grating pitch in order to be in the range of the optimal performance of the NDB encoder [18].

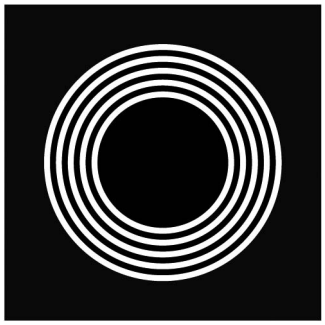

Fig. 2. Binary amplitude DOE designed to produce de NDB.

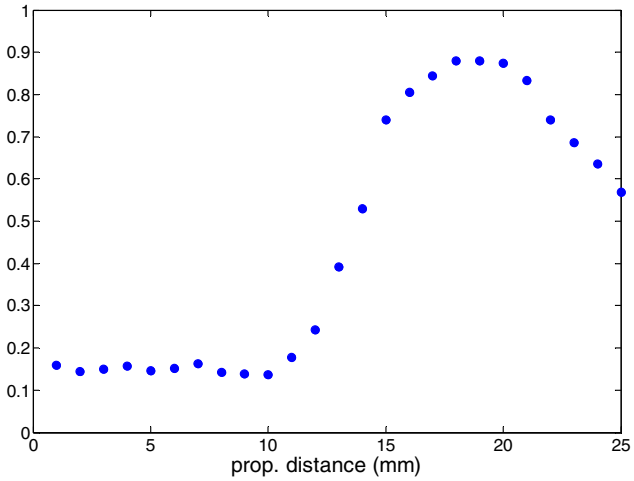

Fig. 3. Correlation coefficient between the simulated NDB produced with the DOE of Fig. 2 at different propagation distances and the theoretical zero-order Bessel beam ($\lambda = 635$ nm).

Figure 4 shows the images of the theoretical (for $r_0 = 15.5$ μm), simulated, and experimental NDBs at a propagation distance of 18 mm from the DOE, for $\lambda = 635$ nm.

B. Photodetector

The photodetector was an application specific integrated circuit (ASIC) specifically designed for this NDB encoder configuration, fabricated in a 0.5 μm CMOS process. A scheme of the photodetection ASIC is shown in Fig. 5. The ASIC detection area consists of a set of eight concentric annular photodiodes. The photodiodes were fabricated as highly n-doped implants on active areas over the epitaxial p-doped substrate. The photocurrent generated at each annular photodiode is multiplied by a programmable weighting factor using current mirrors, and the contributions of each detector are added to produce a signal (IOUT in Fig. 5). The weighting factors can be programmed by a string of configuration data that is stored in a chain of shift registers. This arrangement enables us to synthetize different detectivities: for example, the besinc^2 detectivity required for this application. A complete technical description of this programmable photodetector as well as its response curve can be found in [20].

The profile of the function given by Eq. (5) is represented at the left in Fig. 6 for different values of the size parameter a. To

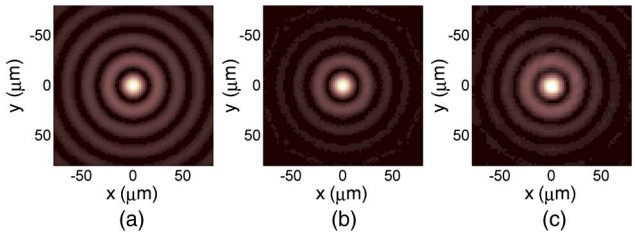

Fig. 4. (a) Theoretical zero-order Bessel NDB. (b) Simulated NDB produced by the DOE of Fig. 2. (c) Image of the NDB produced in the lab by the DOE of Fig. 2.

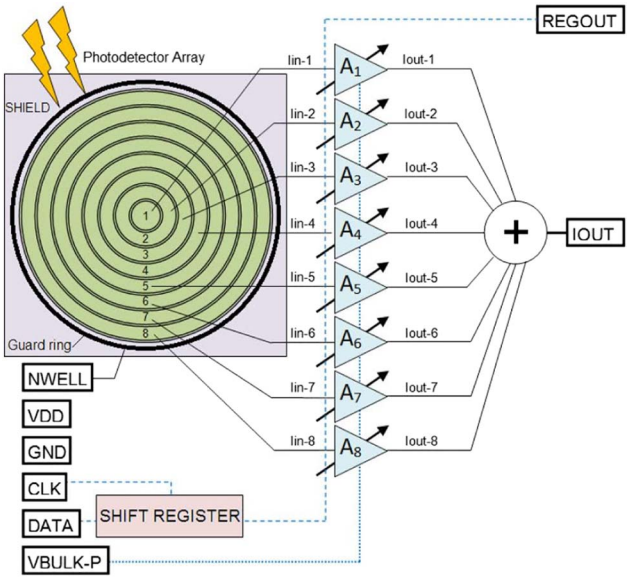

Fig. 5. Diagram of the sensor used in this work, showing the independent programmable gain system for each of the eight annular concentric photodiodes and the output signal, which is the concurrent sum of the eight weighted photocurrents.

implement a detectivity proportional to this function, we proposed to discretize it by using eight circular pixels, that is, eight concentric photodiodes, taking into account the circular symmetry of the *besinc* function. Each pixel has a configurable gain factor between 0 and 63, and the output current is the concurrent sum of all the weighted photocurrents. Each graph at the right of Fig. 6 shows the discretized version of the exact profile of the besinc^2 function represented at the left.

4. EXPERIMENTAL RESULTS AND ANALYSIS

We present in this section the experimental signals obtained with the setup shown in Fig. 1, that is, the photocurrents at the photodetector output as a function of Δx, the relative displacement between the grating and the encoder head. The NDB optical encoder signal was measured using different values of the configuration and experimental parameters: synthesized detector size a, scale–photodetector distance, detector misalignment, and wavelength. As previously stated, our focus is to characterize the electric signal obtained with the scheme configuration of Fig. 1. However, in the final design of the encoder, four similar 90° phase-shifted signals will be required, as previously mentioned.

The first analysis is the dependence on the detector size. Figure 7 shows the photocurrents for 10 different synthesized detectivity functions at the programmable photodetector, as explained in the previous section. We first show the results for the blue laser diode with $\lambda = 405$ nm (Figs. 7–12).

The distance between the scale and the sensor is $z = 0.5$ mm in the particular case in Fig. 7, however, the characteristic photocurrents remains the same for other z values. We were unable to achieve lower values of z because of the sensor chip packaging. As long as the detector size is increased, the mean value of the photocurrent also increases, as expected. Figure 8 shows the signal amplitude and contrast versus the detector size. This graph clearly shows the trade-off between the contrast and the amplitude of the signal to find an optimal detector size.

The experimental results of Figs. 7 and 8 were carried out for several distances z between the grating and the detector. The variation of the signal amplitude with the distance is plotted in Fig. 9, and in Fig. 10 the signal contrast is represented as a function of z.

The effect on the photocurrent of the detector misalignment in the x direction (Fig. 1) with respect to the center of the NDB is represented in Figs. 11 and 12. In the first figure, the signals for the synthesized detector size of $a = 108.5$ μm are shown for misalignments up to 35 μm at $z = 1.135$ mm. The signals preserve their sinusoidal shape, but their amplitudes and contrasts diminish, as is shown in Fig. 12.

Vertical misalignments between the NDB and the photodetector of the same magnitude than lateral misalignments

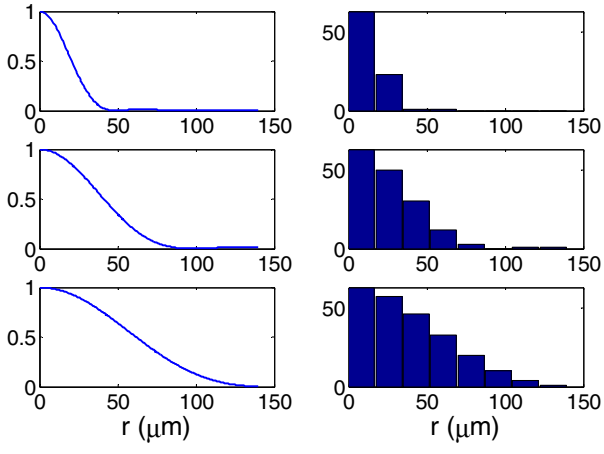

Fig. 6. Radial profile of the detectivity function for three values of the size parameter a (40, 80, and 120 μm, from top to bottom). Exact besinc^2 (left). Gain factor of the eight photodiodes (right) that synthesize the exact detectivity function at the left.

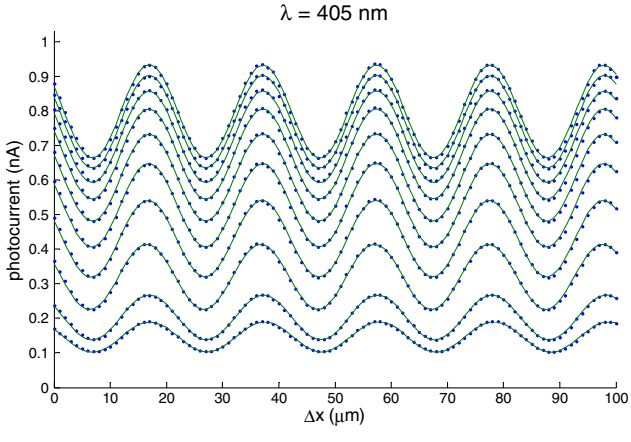

Fig. 7. Photocurrents at the photodetector versus displacement for blue light together with their respective sinusoidal fit. The curves correspond to 10 different values of the synthetized detector size (from bottom to top: $a = 15.5$, 46.5, 77.5, 108.5, 139.5, 170.5, 201.5, 232.5, 263.5, and 294.5 μm).

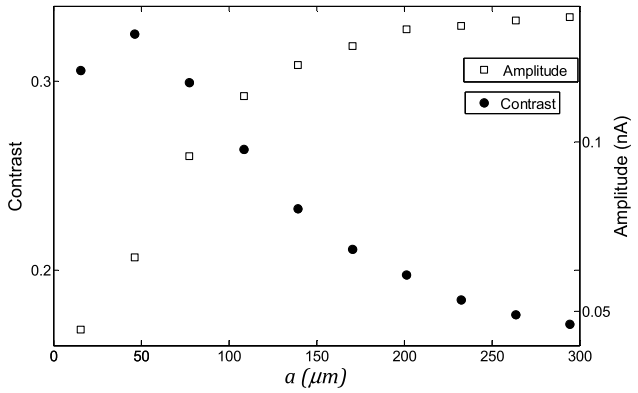

Fig. 8. Contrast and amplitude of the signals in Fig. 7.

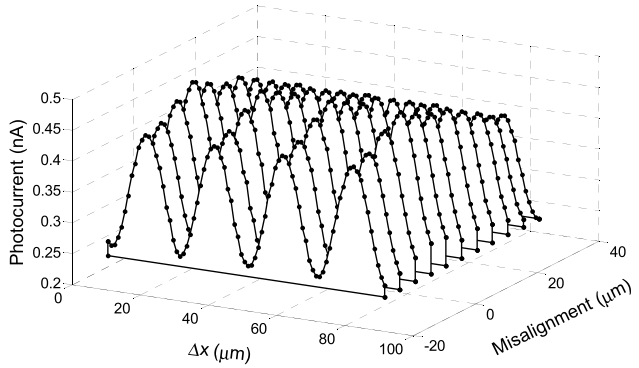

Fig. 11. Photocurrent signals at different misalignments for the synthesized detector size of $a = 108.5$ μm.

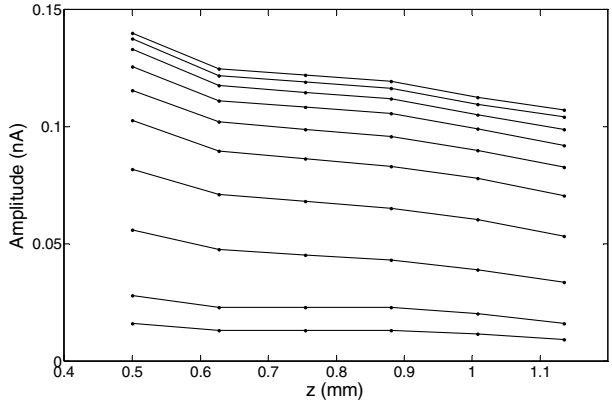

Fig. 9. Signal amplitudes versus detector-scale distance for blue light and different values of a (from bottom to top: $a = 15.5$, 46.5, 77.5, 108.5, 139.57, 10.5, 201.5, 232.5, 263.5, and 294.5 μm).

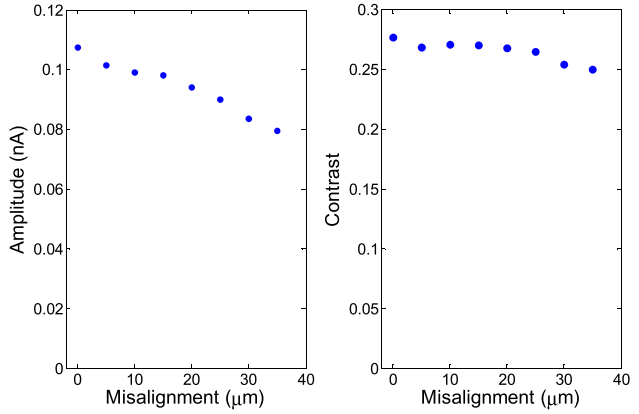

Fig. 12. Amplitude and contrast of the signals in Fig. 11 versus misalignment.

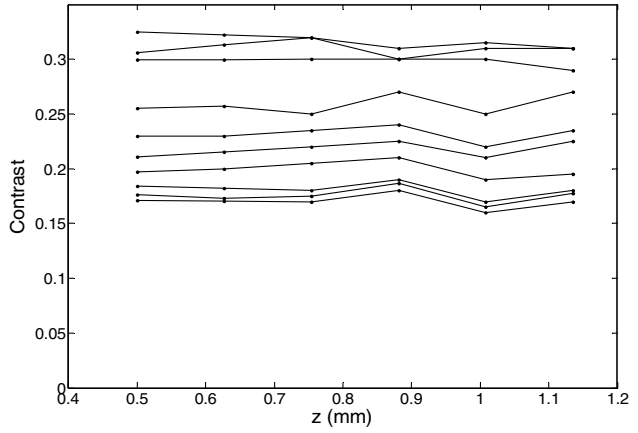

Fig. 10. Signal contrasts versus detector-scale distance for blue light. The different values of a (from top to bottom) are $a = 46.5$, 15.5, 77.5, 108.5, 139.5, 170.5, 201.5, 232.5, 263.5, and 294.5 μm.

of Figs. 11 and 12 cause much lower changes in the photocurrents, a result previously stated in one of our previous works [19].

These experimental results obtained with the blue laser were consistent with the numerical simulations. Anyway, in order to study the cross-talk effects of the photodetection between the annular photodiodes in the integrated circuit, we will now present the results that were obtained using a red laser beam. As later explained in this text, red light has a higher penetration depth in silicon, leading to cross-talk problems among detectors due to the diffusion of minoritary carriers generated below the depletion regions of the photodiodes. The experimental procedure was the same as the one carried out with the blue laser.

Figure 13 shows the photocurrents at the photodetector for different synthesized detector sizes using the red laser. The results were obtained with the same parameters from Fig 7.

The contrasts (Fig. 14) of the signals in Fig. 13 are lower than their equivalents in Fig. 8. For example, the maximum contrast is 0.12 for red light and 0.32 for blue light.

According to the simulations through the propagation of the angular spectrum, these contrast values for red light were not actually expected. To understand the cause of this drop, we repeat the experiment using a CCD camera to capture the images at the plane of the photodetector chip as a function of the displacement Δx. Figure 15 shows two of those images, corresponding to displacements that give maximum and minimum

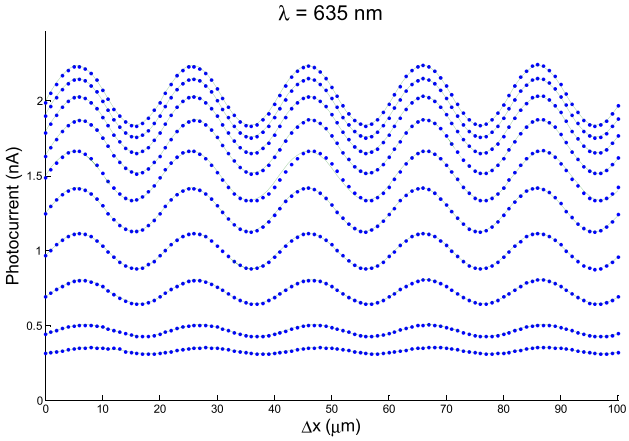

Fig. 13. Same as Fig. 7 but using a red laser diode.

photocurrents. Then, we associate a gain factor to each pixel according to the corresponding gain factor of each annular photodiode that synthesizes a particular size of the besinc^2 detectivity function. The sum over all the pixels must give, therefore, a number proportional to the expected photocurrent at the chip for the same synthesized size parameter at the same Δx. With these values, we then calculate the contrast as a function of the synthetized size parameter (Fig. 16).

Comparing the contrasts represented in Figs. 14 and 16, the following details are highlighted: the maximum contrast in Fig. 16 doubles the higher contrast in Fig. 14; the differences are important for the smaller values of the parameter a, and, as long as the synthesized detector size increases, the differences between the contrasts diminish. We attribute these differences to the differences in the cross talk for different wavelengths.

CCD technologies make use of low-doped deep epitaxial layers where charge generation and collection occur, and the large voltage drive (10–15 V) results in electric field action in regions extending up to 7–10 μm in the substrate. In contrast, the CMOS process is made of a thin epi-layer on low-resistivity substrate and uses a low-voltage drive, thus giving an electric field action extending only to 1.2 μm in the silicon depth; consequently, charges will have to diffuse to be collected. The penetration depths of blue (405 nm) and red (635 nm)

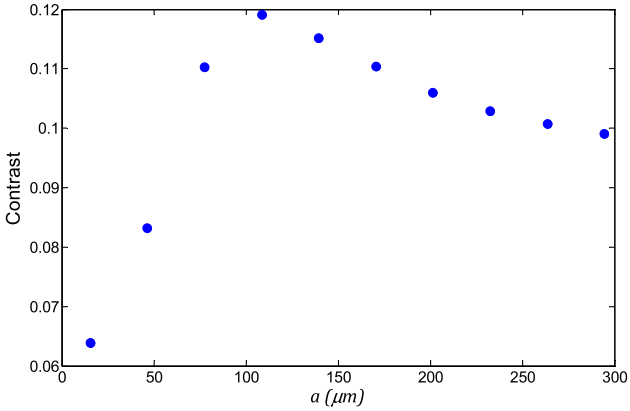

Fig. 14. Contrast of the signals in Fig. 13.

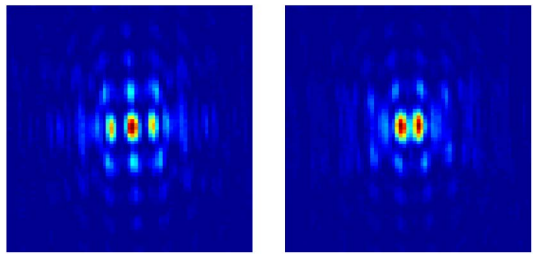

Fig. 15. Images at the photodetector plane ($z = 0.5$ mm) for displacements corresponding to maximum (left) and minimum (right) photocurrents.

photons are 0.17 and 3.3 μm, respectively [28]. Therefore, the red photons are generating electron-hole pairs in all the substrate, in a much deeper zone than the junction and the depletion region. These carriers can reach any photodiode by diffusion and cause, consequently, the programmed gain factors of the eight photodiodes to not synthesize adequately the intended detectivity function. This behavior is not observed for blue light because its penetration depth is only 0.17 μm. The fact that the differences for red light between the contrasts obtained with the sensor chip and with the CCD diminish, as long as the synthesized detector size increases, is also consistent with the cross talk: an increasingly large synthesized detector size appears to be more and more like a monolithic photodetector, which, of course, has no cross talk.

In addition, the contrast for blue light versus a (Fig. 8) has the same functional shape than the one for the red light taken with the CCD camera; however, the contrast for red light is still a little lower. This is due to the fact that the distance z at which the contrast has a maximum is not the same for different wavelengths [18].

The electronic interpolation ability of the encoder is related to the harmonic content of the signal. Figure 17 shows the spectral amplitude of one of the photocurrent signals of Fig. 7, thus indicating that it is always below 1% of the spectral amplitude at the grating frequency (50 mm^{-1}). The simulation through the propagation of the angular spectrum (not shown in Fig. 17) provides good estimation of the harmonic content [13] but predicts null intensity at frequencies other than multiples

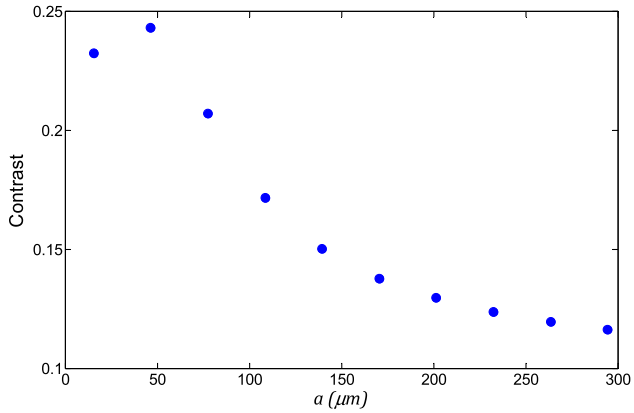

Fig. 16. Contrast of the signals obtained with the CCD images for a red light at $z = 0.5$ mm.

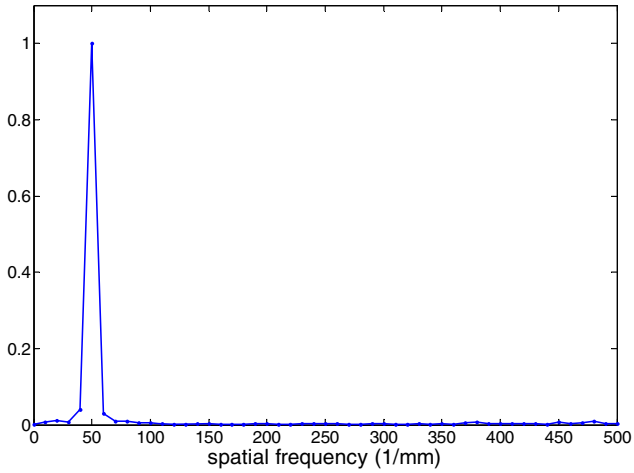

Fig. 17. Normalized spectral amplitude of one of the signals of Fig. 7 ($a = 108.5$ μm).

of the grating frequency; therefore, the spectral noise of the experimental results reveals that the grating used in the lab had some minor imperfections.

5. CONCLUSIONS

We present in this work an implementation of an optical encoder based on a nondiffractive beam, which generates an appropriate incremental signal. This implementation is done with a 20 μm Ronchi grating and includes two specially designed elements: a diffractive optical element (to produce the quasi-nondiffractive beam) and a programmable gain CMOS structured detector (to synthesize the most convenient detectivity function).

The setup was mounted, and a comprehensive analysis of its performance was done. The system generates an incremental signal with good contrast and low harmonic content. Different sizes of besinc^2 detectivity functions were programmed on the CMOS photodetector, thus allowing us to experimentally verify the most suitable detector size. The stability of the signal under variations of the detector-grating distance is superior to the standard mounting tolerances in that direction (0.1 mm typically) due to the intrinsic propagation invariance of the NDBs. In addition, the detector can be placed as close as needed to the grating.

The signal contrast significantly decreases when red light is used instead of blue light. It was stated that the cross talk between the annular photodiodes is responsible for this effect.

The intrinsic resolution of the system is equal to the grating pitch, which 20 μm; however, according to the obtained signal characterization, it is estimated that an electronic interpolation up to a hundredth of the grating pitch is attainable. The reason is that, for a 0.1 mm variation in the detector-grating distance, the change in the signal amplitude is less than 5% (depending on the chosen working distance); for that amplitude variation, the maximum interpolation error is 0.2 μm [21]. The harmonic content of the signal is less than 1%, the maximum interpolation error it produces is less than 0.05 μm. In order to properly calculate the interpolation ability of the optical encoder based on a nondiffractive beam, it is necessary to produce the four 90° phase-shifted incremental signals because the interpolation error depends also on the offset and the phase shifts of these four signals. The pitch, yaw, and roll tolerances also must be evaluated with the complete optical head design that will be able to produce the four signals.

It was shown (Fig. 12) that a few tens of micrometers of misalignment produce a signal amplitude variation that would undermine the interpolation ability. Thus, the most expensive part of this encoder is the man-hours needed to align the detector with the laser diode and the DOE. In order to reduce this cost, we are now working on the development of a pixelated detector with self-centering capabilities.

According to the conclusions of the two preceding paragraphs, the future work will be directed to integrate in the encoder head the four NDB and detectors to obtain the two quadrature signals with zero mean and to automatize the detector alignment with respect to the NDB axis.

Funding. Agencia Nacional de Promoción Científica y Tecnológica (National Agency for Science and Technology, Argentina) (PICT2008-0077, PICT2013-0951).

REFERENCES

1. L. Wronkowski, "Diffraction model of an optoelectronic displacement measuring transducer," Opt. Laser Technol. **27**, 81–88 (1995).
2. D. Crespo, J. Alonso, and E. Bernabeu, "Reflection optical encoders as three-grating moiré systems," Appl. Opt. **39**, 3805–3813 (2000).
3. D. Crespo, J. Alonso, T. Morlanes, and E. Bernabeu, "Optical encoder based on the Lau effect," Opt. Eng. **39**, 817–824 (2000).
4. G. Swanson and E. Leith, "Analysis of the Lau effect and generalized grating imaging," J. Opt. Soc. Am. A **2**, 789–793 (1985).
5. D. Crespo, J. Alonso, and E. Bernabeu, "Experimental measurements of generalized grating images," Appl. Opt. **41**, 1223–1228 (2002).
6. F. J. Torcal-Milla, L. M. Sanchez-Brea, and E. Bernabeu, "Double grating systems with one steel tape grating," Opt. Commun. **281**, 5647–5652 (2008).
7. W. Huber and M. Allgauer, "Interferential linear and angular displacement apparatus having scanning and scale grating respectively greater than and less than the source wavelength," U.S. patent 5,424,833 (13 June 1995).
8. C.-C. Wu, W.-J. Wu, Z.-S. Pan, and C.-K. Lee, "Laser linear encoder with both high fabrication and head-to-scale tolerances," Appl. Opt. **46**, 3169–3176 (2007).
9. C.-F. Kao, S.-H. Lu, H.-M. Shen, and K.-C. Fan, "Diffractive laser encoder with a grating in littrow configuration," Jpn. J. Appl. Phys. **47**, 1833–1837 (2008).
10. F. Perez-Quintian, A. Lutenberg, and M. A. Rebollo, "Linear displacement measurement with a grating and speckle pattern illumination," Appl. Opt. **45**, 4821–4825 (2006).
11. H. Miyajima, E. Yamamoto, M. Ito, S. Hashimoto, I. Komazaki, S. Shinohara, and K. Yanagisawa, "Optical micro encoder using a vertical-cavity surface-emitting laser," Sens. Actuators A Phys. **57**, 127–135 (1996).
12. J. Akedo, H. Machida, H. Kobayashi, Y. Shirai, and H. Ema, "Point source diffraction and its use in an encoder," Appl. Opt. **27**, 4777–4781 (1988).
13. A. Lutenberg, F. Perez-Quintian, and M. A. Rebollo, "Optical encoder based on a non-diffractive beam," Appl. Opt. **47**, 2201–2206 (2008).

14. H. S. Lee and S. S. Lee, "Reflective optical encoder capitalizing on an index grating imbedded in a compact smart frame," IEEE Photon. J. **6**, 6800908 (2014).
15. S. Nagai, T. Sasaki, H. Kawaguchi, A. Iwabuchi, and K. Hane, "Monolithic displacement encoder sensor integrating GaN LED and Si photodiodes," in *Proceedings of IEEE Transducers*, Barcelona, Spain, 16–20 June 2013.
16. http://www.heidenhain.com/fileadmin/pdb/media/img/208960-2C_Exposed_Linear_Encoders.pdf.
17. http://www.renishaw.com/media/pdf/en/a76a7e13ca474c538f1ff1f9e301418b.pdf.
18. A. Lutenberg and F. Perez-Quintian, "Optical encoder based on a nondiffractive beam II," Appl. Opt. **48**, 414–424 (2009).
19. A. Lutenberg and F. Perez-Quintian, "Optical encoder based on a nondiffractive beam III," Appl. Opt. **48**, 5015–5024 (2009).
20. N. Calarco, F. Perez Quintian, A. Lutenberg, and J. Lipovetzky, "Design of a customized CMOS active pixel sensor for a non-diffractive beam optical encoder II," in Proceedings of the *7th Argentine School Micro-Nanoelectronics, Technology and Application*, Buenos Aires, Argentina, 2011, pp. 62–65.
21. L. M. Sanchez-Brea and T. Morlanes, "Metrological errors in optical encoders," Meas. Sci. Technol. **19**, 115104 (2008).
22. Z. Bouchal and M. Olivik, "Non-diffractive vector Bessel beams," J. Mod. Opt. **42**, 1555–1566 (1995).
23. J. Goodman, *Introduction to Fourier Optics*, 3rd ed. (Roberts & Company, 2005).
24. J. E. Durnin, "Exact solutions for nondiffracting beams. I. The scalar theory," J. Opt. Soc. Am. A **4**, 651–654 (1987).
25. J. Durnin, J. J. Miceli, and J. H. Eberly, "Diffraction-free beams," Phys. Rev. Lett. **58**, 1499–1501 (1987).
26. J. Turunen, A. Vasara, and A. T. Friberg, "Holographic generation of diffraction-free beams," Appl. Opt. **27**, 3959–3962 (1988).
27. R. M. Herman and T. A. Wiggins, "Production and uses of diffraction-less beams," J. Opt. Soc. Am. A **8**, 932 (1991).
28. J. Nelson, *The Physics of Solar Cells* (Imperial College, 2003).